Journal of Flow Chemistry (2023) 13:31–44
https://doi.org/10.1007/s41981-022-00251-z

FULL PAPER

Reactor performance estimation in microscale flow calorimeter for rapid characterization of exothermic reactions

Timothy Aljoscha Frede[1] · Nick Nikbin[1] · Norbert Kockmann[1]

Received: 26 October 2022 / Accepted: 24 November 2022 / Published online: 12 December 2022

Abstract

Continuous flow calorimeters are a promising tool in process development and safety engineering, especially for flow chemistry applications to characterize the heat release and kinetic parameters of rapid chemical reactions. In this study, the digital accompaniment of an isoperibolic flow calorimeter for characterization of exothermic reactions is presented. To support experimental planning and evaluation, computational fluid dynamic simulations are carried out for single-phase flow in the microreactor. The residence time distribution is obtained and used for estimation of conversion and temperature profiles along the microreactor channel. This leads to an integration of CFD simulations into the calorimeter's software-guided workflow reducing the experimental effort regarding the determination of thermokinetic data. The approach is tested for a highly exothermic test reaction, which provides further hints for future investigations.

Article highlights

- Estimation of conversion and temperature profiles within a microscale calorimeter
- Combination of CFD simulations and reactor performance estimation
- Approach was tested for highly oxidation of sodium thiosulfate
- Estimated conversion and temperature profiles are in good agreement with experimental data

Keywords CFD simulation · Compartment Modeling. · Design of Experiments. · Digital Twin. · Flow Calorimetry. · Microreactor.

Introduction

Flow calorimetry with software-guided workflow is a promising tool for fast and reliable characterization of highly exothermic reactions with respect to their thermodynamic and kinetic parameters. Traditionally, these parameters are determined by a series of experiments in batch reactors. Batch experiments are not advantageous for both safety and economy considerations, as comparatively large reactor volumes are involved. This creates an urgent for methods to assess thermokinetic data based on microscale experiments. Experimental and numerical investigations of hydrodynamics and chemical reactions in microstructured devices have been widely published in literature. For example, Moore and Jensen [1] presented transient flow experiments using residence time or temperature ramps to accelerate determination of kinetic data [2]. The steady state needs no longer to be waited for, saving both long and material-intensive experimentation. However, these experiments are linked to the connection of process analytical technology tools to the microreactor to determine conversion. The method has been applied with various analytical procedures such as Raman measurements [3, 4], HPLC analysis [5–7] and FTIR measurements [8, 9].

Continuous flow calorimetry enables to estimate reaction conversion from the heat released. Especially, spatially resolved reaction calorimetry, as developed by several groups

✉ Timothy Aljoscha Frede
Timothy.Frede@tu-dortmund.de

✉ Norbert Kockmann
Norbert.Kockmann@tu-dortmund.de

[1] Department of Biochemical and Chemical Engineering, Laboratory of Equipment Design, TU Dortmund University, Emil-Figge-Straße 68, 44227 Dortmund, Germany

[10–18], allows to follow the reaction progress along the reaction channel and enables thermokinetic characterization of chemical processes. Despite the recording of spatially resolved heat flux profiles, the calorimetric measurement data were often only used for an energy balance of the system to determine the enthalpy of reaction. Schneider and Stoessel [19] presented a calorimetric method to determine global kinetics of exothermal reactions and their activation energy. The conversion at the reactor outlet was estimated by setting the measured heat flux in relation to the heat flux at complete conversion.

To overcome challenges related to experimental measurements and to optimize real processes, the systematical use of simulation tools such as computational fluid dynamics (CFD) is essential. The meaningful combination of CFD and experiments to evaluate reactor performance has been described by several groups [20–23]. To reduce model complexity for the CFD models, the compartment modeling approach has been applied and proved for different applications. A review on compartmental modeling and its application in chemical engineering is provided by Jourdan et al. [24] Cremer-Bujara et al. [25] used the compartment modeling approach as a combined approach between CFD models and axial dispersion models for the simulation of polymer reactors. In their work, the compartments were determined based on the periodicity of velocity fields within a static mixer reducing model complexity and computational effort.

In this work, the compartment modeling approach is used combining CFD simulations and reactor performance estimation. The focus here is put on the simplification and acceleration of estimation of temperature and conversion profiles of fast and exothermic reactions within microreactors. The coupling of CFD and reactor performance estimation is shown for the oxidation of sodium thiosulfate (NaTS) using hydrogen peroxide (HP) as a test reaction and compared to experimental data determined in our microcalorimeter [26]. This leads to an integration of CFD simulations into a microcalorimeter's software-guided workflow reducing the experimental effort regarding the determination of thermokinetic data.

Materials and methods

The investigated microreactor is presented with its geometry and flow fields as they build the basis of the simulations. The hydrodynamics with steady state simulations are described with the meshes used for discretization of the flow fields and their verification. The reactor performance estimation is explained, which is based on the residence time distribution (RTD) from the CFD simulations and reaction kinetics. Finally, the investigated single-phase liquid reaction and its thermokinetic parameters are provided. The thermokinetic parameters are utilized in the reactor performance estimation.

Microreactor

A commercially available microreactor from Little Things Factory GmbH (Elsoff, Germany) is investigated in the simulations. The LTF-MS reactor from the MR-Lab series is studied in this work, which is the scale-up version of the LTF type-S reactor, which was employed in the microcalorimeter in previous works [14, 15, 27]. A schematic representation of reactor is shown in Fig. 1.

Khaydarov et al. [22] also investigated the LTF-MS reactor regarding its mixing performance using CFD and experiments for validation. Additionally, the reactor is currently employed in the microcalorimeter enabling a validation with experimental data [26]. The reactor consists of two straight inlet channels, which merge in a Y-mixer, followed by a chicane mixing geometry with eleven identical mixing elements. The outlet is connected to a residence time channel with two 90° bends. The total internal volume is 0.24 mL. The axial reactor channel length is approximately 260 mm.

Numerical modeling with CFD

Governing physical equations

In case of incompressible steady state liquid flow without any sink or source, the continuity equation can be simplified to Eq. 1.

$$\rho_l \vec{\nabla} \cdot \vec{u} = 0 \Leftrightarrow \vec{\nabla} \cdot \vec{u} = 0 \tag{1}$$

The liquid's density is represented by ρ_l and $\vec{u}$ is the velocity vector. The momentum transport in continuum mechanics is described by the Navier-Stokes equation, Eq. 2.

$$\rho_l \frac{\partial \vec{u}}{\partial t} + \rho_l \left(\vec{u} \cdot \vec{\nabla} \right) \vec{u} = -\vec{\nabla} p + \eta_l \Delta \vec{u} + \vec{f} \tag{2}$$

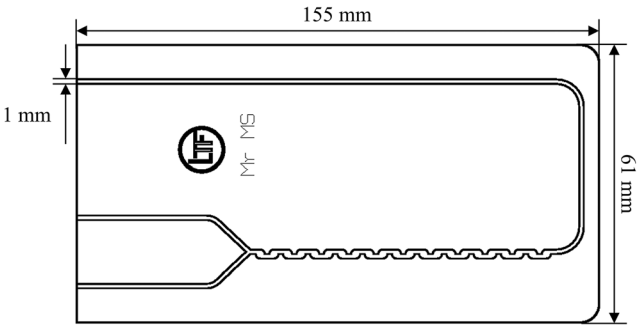

Fig. 1 Schematic representation of LTF-MS reactor from Little Things Factory GmbH. Reproduced with permission of LTF, Elsoff, Germany

In addition to the definitions in Eq. 1, p describes the pressure and η_l the dynamic viscosity of the fluid. Volumetric forces such as the gravitational force are symbolized by $\vec{f}$. In micro process engineering, gravitational forces can be neglected compared to other forces in microchannels such as surface tension [28]. Hence, the Navier-Stokes equations simplify to Eq. 3 for incompressible steady state fluid flow in micro channels.

$$\rho_l\left(\vec{u}\cdot\vec{\nabla}\right)\vec{u} = -\vec{\nabla}p + \eta_l\Delta\vec{u} \tag{3}$$

The numerical solution of the simplified Navier-Stokes equation is performed in ANSYS CFX, version 2021 R1.

Mean age theory

The so-called *Mean Age Theory* can be used to spatially derive mean residence time within steady state flow fields. Thus, computational effort for the mean age simulations is orders of magnitude lower than for transient simulations. In addition, a contour plot of the mean age visualizes size and locations of flow regions such as short circuiting or dead zones more intuitively than RTD function or a velocity vector plot. The term "*age*" is reserved for the elapsed time since entrance of a fluid particle as a tracer, which still reside in the reactor. When a fluid particle exits the channel volume, its age equals to its residence time. The derivation of the age distribution is based on the governing equations derived by Spalding, Sandberg, Liu and Tilton [29–31]. Eq. 4 shows the transport equation for a tracer species, where D is the molecular diffusion coefficient. With integration and use of spatial invariants, Eq. 5 is acquired, which describes the conservation equation for mean age for incompressible flows.

$$\frac{\partial c}{\partial t} + \nabla\cdot(uc) = \nabla\cdot(D\nabla c) \tag{4}$$

$$u\cdot\nabla\alpha = \nabla\cdot D\nabla\alpha + 1 \tag{5}$$

Since Eq. 4 has the same form as steady-state transport equation for momentum, energy, and species, it can be solved with the same CFD-solver.

To resolve local tracer concentrations spatially, one can use the spatial age distribution function, given in Eq. 6. Here, $\widetilde{f}(x,\alpha)$ is the frequency distribution of the age α of molecules at the local point of interest x. The mean age can be described by Eq. 7.

$$\widetilde{f} = \frac{c(x,\alpha)}{\int_0^\infty c(x,t)dt} = \frac{d\widetilde{F}}{d\alpha} \tag{6}$$

$$\alpha(x) = \frac{\int_0^\infty tc(x,t)dt}{\int_0^\infty c(x,t)dt} = \int_0^\infty tdt \tag{7}$$

A detailed description to implement the mean age theory in ANSYS CFX is given in [32].

Numerical model

A computer-aided design model was generated using ANSYS SpaceClaim. The model was divided into several compartments. Since the compartments are much smaller than the overall geometry, fewer grid elements are necessary for discretization, too. In Fig. 2, the compartments of the LFT-MS reactor are presented.

With the exception of the mixing geometry, the compartments are chosen to match the areas of the heat flux sensors used in our experimental setup [26]. Thus, experimentally determined heat transfer coefficient can be used for those reactor parts. A symmetry plane in z-direction is used for the entire microreactor reducing the model size by half and the solution time by 25%. The chicane mixing elements were split into parts of one and a half of an element to account for back mixing in axial direction, as shown in Fig. 2.

All simulations share the same boundary conditions. Fully developed velocity profiles are set at the inlets as they showed more accurate behavior than plug flow profiles [33]. The velocity is calculated from the prescribed volumetric flow rate. At the walls, no slip condition is set with zero flux. Symmetry regions are assigned in the meshing process and are allocated in CFX-Pre. The average static pressure is set to zero over the entire outlet to force continuing flow to the next reactor compartment. A precursor plane is embedded between the end of the mixing element and the beginning of the next element. From here, the boundary profiles at the outlet are obtained and reused in the next compartment as inlet conditions, as shown in Fig. 3.

The process is repeated until the entire microreactor is represented for the numerical simulation. A mixture of two identical parts of water is used as a fluid, since aqueous solutions are used in the experiments. The physical properties of water are assumed with a density of ρ_l= 997 kg m^{-3}, a diffusion coefficient of D= 9.57·10^{-10} m^2 s^{-1} and a dynamic viscosity of η_l= 8.899·10^{-4} kg m^{-1} s^{-1}.

The compartments were meshed by ANSYS Workbench. Usually, tetrahedrons or hexahedrons are used to generate a grid corresponding to the problem, since they are suitable to approximate complex geometry. In general, grids can be structured or unstructured. Unstructured grids are built without a fixed topology. Cells can have different sizes and forms, which allows for local grid refinement. In complex geometries, such as bends and curves, it is possible to obtain a higher resolution and therefore a higher quality of results. In conclusion, unstructured grids are flexible and can be generated automatically with most CFD software, which makes them an interesting choice for complex flow fields. A disadvantage of unstructured grids is the higher computational effort required

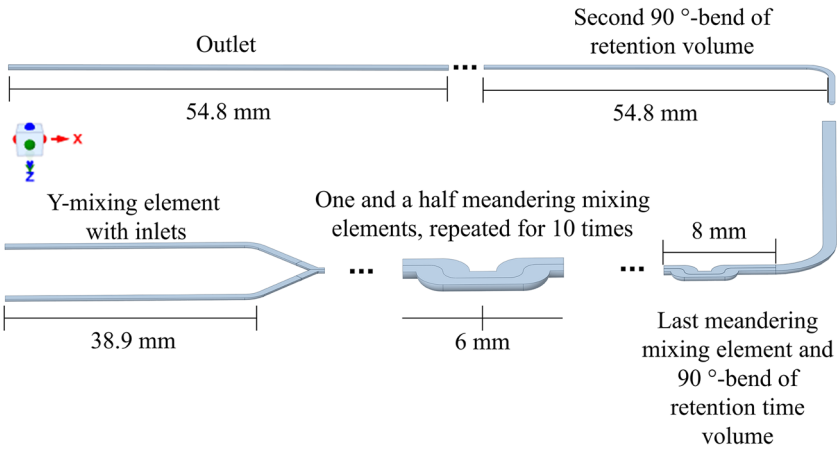

Fig. 2 Compartments of the flow domain for the LTF-MS reactor, designed with ANSYS SpaceClaim

to solve the flow field compared to structured ones, since the matrix of algebraic equations is irregular and more difficult to solve. Modern mesh generation tools allow the use of prism layers near the boundaries of the solution domain. The mesh is then unstructured along the wall but layered and almost orthogonal in wall-normal direction. Thus, boundary layers can be calculated more accurate. [34]

An unstructured grid, consisting of tetrahedral elements and prism layers at the walls is chosen as grid type to ensure a higher flexibility for the simulation of the meandering channel. Prism layers are applied for an accurate description of the gradients at the wall. The number and arrangement of elements on the edges is fixed. This is necessary for of the transfer of boundary profiles between the reactor compartments. The simulations for the grid independence were performed for

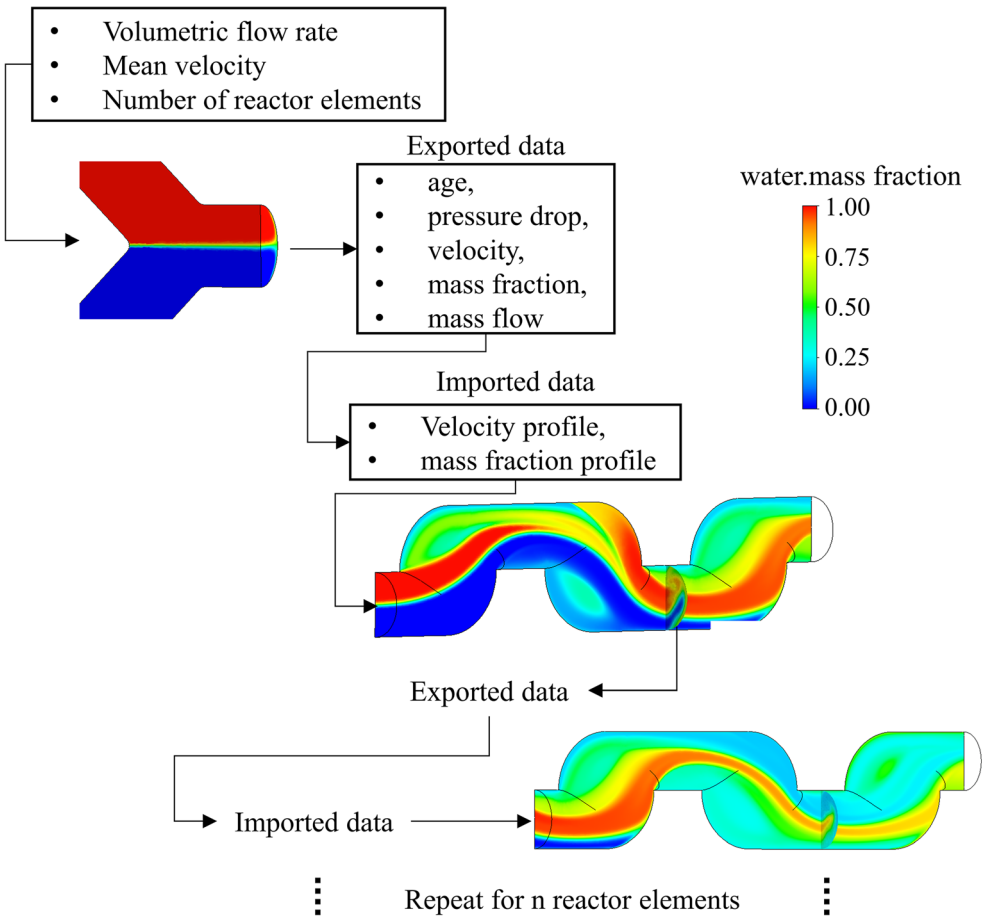

Fig. 3 Automation routine visualized for the LTF-MS reactor at $\dot{V}$ = 12 mL min^{-1}

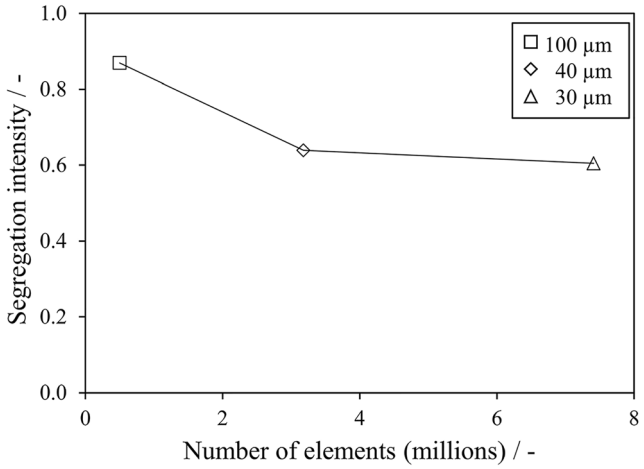

Fig. 4 Segregation intensity at the outlet of the second mixing element for three differently sized grids with 100, 40 and 30 µm large grid elements

a volumetric flow rate of $\dot{V}$ = 12 mL min^{-1} and three numerical grids with the refinement steps of 100, 40 and 30 µm. Danckwerts' segregation intensity [35] after the second mixing element was used for evaluation of grid independence, as shown in Fig. 4.

It is evident that the segregation intensity converges for the third grid with a cell size of 30 µm and nearly 7.4 million grid elements. Doubling the number of elements from the second grid to the third grid leads to a deviation of 5.77%. This is considered small enough to treat the solution of the third grid as converged. In addition, it is sufficient for the methods in this work. However, a finer grid is recommended for more accurate, quantitative calculations. The grid of the whole LTF-MS reactor features nearly 32 million elements with an element size of 30 µm. The corresponding grid is shown exemplarily for the mixing element in Fig. 5.

The properties of the chosen grid and rating criteria for the numerical grid are given in the supplementary information (SI).

Solver settings

The coupled solver in ANSYS CFX is used to acquire the solutions of the isothermal, laminar and incompressible flow system. In general, the computational effort for such solvers is higher than with iterative solvers, but the solution is acquired comparatively faster. The CFX solver runs in parallel mode to reduce the simulation time. To obtain accurate results with iterative solvers it is important to control the simulation errors. The following solver control settings are used:

- high resolution advection scheme,
- residual type RMS smaller than 10^{-5},
- conservation target of mass, momentum, and mass fraction of 0.01,
- residuals for the additional variable *age* of 10^{-4}.

With these settings, the following results were achieved.

Reactor performance estimation

The aim of the reactor modelling is to predict reactor performance to support experimental planning. If the reactor performance is estimated, the number of experiments can be reduced to set-points, where calorimetric measurements are suitable with

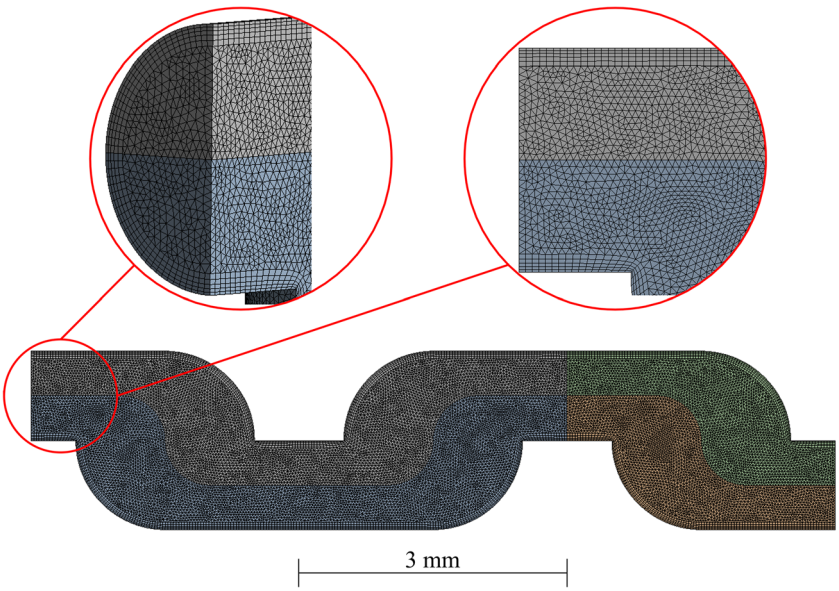

Fig. 5 Numerical grid of a mixing element of the LTF-MS reactor with tetrahedral elements and prism layers at the walls

continuous reaction calorimeters. A prediction of reactor behavior is possible with residence time data, a chosen reactor model and the reaction kinetics [36]. Hence, the next step is the prediction of reactor behavior using the obtained residence time data from CFD linking it with a suitable reactor model. For irreversible reaction of first order, the conversion in a reactor can be determined with known residence time, because only in this type of reaction is the chemical behavior of a small fluid element independent of what happens next to it. Thus, there is an undisturbed superposition of residence time behavior $E(t)$ and the course of the reaction $X(t)$, as shown in Eqs. 8 and 9. Eq. 9 applies to the conversion for a first order reaction. [37, 38]

$$\frac{d\overline{X}}{dt} = X(t)E(t) \tag{8}$$

$$\frac{c_A}{c_{A0}} = 1-X \approx \sum_i E(t_i) e^{-kt_i} \Delta t_i \tag{9}$$

Here, $E(t)$ represents the residence time distribution and quantifies the set of fluid elements leaving the reactor at time t matching the frequency distribution of the age.

If the reaction order is non-linear ($m_i \neq 1$), calculations based solely on the RTD are not sufficient anymore. Here, mixing effects play an important role and must be considered additionally. Therefore, hydrodynamic reactor models need to be implemented. In this work, the segregation model is used as it predicts the upper bound of conversion for reaction orders greater than one and less than zero [36, 39]. For total segregation, every volume element in the reactor can be assumed as a small batch reactor. Conversion and product distribution at the reactor outlet are solely dependent on the time spent in the reactor. The probability of the age of a tracer is given by the RTD at the outlet. With this, it is possible to calculate the mean conversion as the integration of all volume elements with different ages at the outlet independent of reaction kinetics using Eq. 8.

Mean conversion

Fluids only react when they are contacted. Thus, the first location of interest is the contact volume in the Y-mixing element. The balance area of Y-mixer is visualized in Fig. 6a.

The balancing area is assumed as a plug flow reactor with a diameter of 1 mm and a length of 1.75 mm. Since laminar flow prevails in the microreactor, the Y-mixer is modeled as a laminar flow reactor (LFR). The analytical solution for the mean conversion a second order reaction in a LFR is given in Eq. 10. [38]

$$\overline{X} = Da\left[1-\frac{Da}{2}\ln\left(1+\frac{2}{Da}\right)\right] \tag{10}$$

The dimensionless Damköhler number Da ist calculated according to Eq. 11 [38].

$$Da = \tau_h k c_0 \tag{11}$$

Mean conversion in the periodic mixing elements is estimated using Eq. 9 with the segregation model due to the complex channel geometries and the assumed deviations from classic reactor models. The balancing scope is shown in Fig. 6b. The distribution function $E(t)$ and the mean residence time τ are derived from the mean age distributions. Next to the distribution function, the conversion rate $X(t)$ is implemented by first order kinetics for the respective reaction with Eq. 9. The conversion rate in a PFR can be calculated with Eq. 12 for further reaction systems with second-order kinetics.

$$X(t) = \frac{kc_{A0}t}{1+kc_{A0}t} \tag{12}$$

Numerical integration of $E(t)$ and $X(t)$ enables the calculation of the conversion profile along the microreactor channel. Since exothermic reactions are investigated here and the heat release depends on the conversion, the conversion profile is used in the following to estimate the temperature in the microreactor channel depending on a selected kinetics.

Heat effects

Since exothermic reactions are investigated with the microcalorimeter, heat effects must be considered. An iterative calculation method is applied to predict the mean conversion and temperature profiles in each reactor compartment. For each iteration, the results of the previous reactor element are inserted into the calculations of the current compartment. This process is repeated until the conversion and temperature profile over the entire reactor is estimated. Figure 7 visualizes this process with the example of a periodic mixing element.

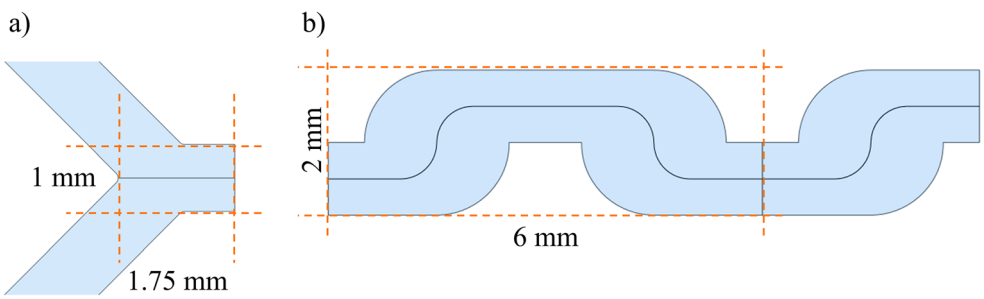

Fig. 6 **a** Balance area of Y-mixing compartment of LTF-MS reactor **b** Balance area of periodic mixing element of LTF-MS reactor

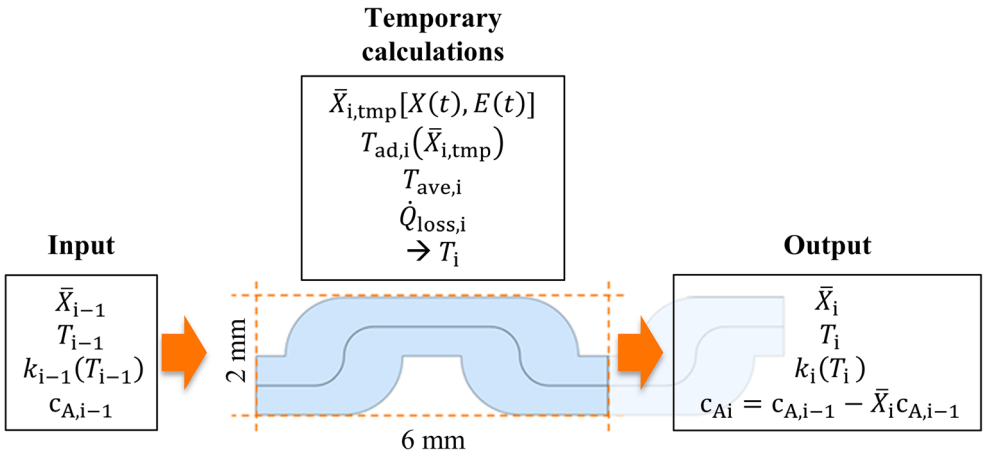

Fig. 7 Iterative calculation steps for the estimation of mean conversion and temperature in periodic mixing element

In the first iteration, a temporary value of $\overline{X}_{i,tmp}$ is calculated at the outlet of the reactor compartment. The calculation depends on the underlying model, as described in the previous chapter. The conversion depends on the reaction rate coefficient for exothermic reactions. Therefore, $k(T)$ is calculated based on the inlet temperature of the compartment T_{i-1}, which is the outlet temperature of the previous compartment. With the temporary value of $\overline{X}_{i,tmp}$, the adiabatic temperature rise due to the reaction is calculated at the outlet of the reactor compartment i with Eq. 13. To include the temperature increase over the whole reactor compartment, the temperature is averaged between the inlet temperature T_{i-1} and the adiabatic temperature $T_{ad,i}$, as shown in Eqs. 13 and 14.

$$T_{ad,i} = T_{i-1} + \frac{(-\Delta H_r)c_{A,i-1}}{c_p}\overline{X}_{i,temp} \tag{13}$$

$$T_{ave,i} = \frac{(T_{ad,i} + T_{i-1})}{2} \tag{14}$$

The specific heat capacity of water is assumed with a constant value of $c_p = 4.1813$ kJ kg^{-1} K^{-1} because it allows for a direct calculation of the outlet temperature, while the errors of neglecting the temperature dependency are considered as small. Heat losses are implemented by applying Eqs. 15 and 16.

$$\dot{Q}_{loss,i} = (T_{ave,i} - T_{ambient})k_{ht,i} \tag{15}$$

$$T_i = T_{ave,i} - \frac{\dot{Q}_{loss,i}}{\rho c_p \dot{V}} \tag{16}$$

Here, k_{ht} represents the respective heat transfer coefficient multiplied by the corresponding heat transfer area of the reactor compartment. The values of k_{ht} are provided by experiments for the type-MS reactor and utilized for a more accurate comparison to conducted experiments. In Eq. 16, the average temperature $T_{ave,i}$ is used as it is also used in the heat loss calculation to account for the mean temperature profile across the reactor compartment. In the second iteration, the reactor compartment temperature T_i is used in Eq. 17 to calculate the reaction rate coefficient $k_i(T)$, which includes the effects of the reaction over the reactor compartment resulting in a higher accuracy.

$$k_i(T) = k_{i-1}(T)e^{\left(\frac{E_A}{R}\left(\frac{1}{T_{i-1}} - \frac{1}{T_i}\right)\right)} \tag{17}$$

To accelerate the predictions of mean conversion and temperature profiles over the entire reactor, the calculations are performed and automated with a Python script. It enables a quick variation of input parameters, such as inlet concentration and inlet temperature to further specify the suggested range of suitable experimental settings.

Case study: Oxidation of sodium thiosulfate

The highly exothermic oxidation of sodium thiosulfate with hydrogen peroxide is used as a single-phase liquid test reaction. Despite the advantages such as non-poisonous, easy and cheaply available components, the thermokinetics and reaction mechanism are still not fully investigated. However, the reaction mechanism with a constant pH-value, shown in Eq. 18, seems most likely and is sufficient for the development of the performance estimation. [40]

$$2\,S_2O_3^{2-} + 4\,H_2O_2 \rightarrow S_3O_6^{2-} + SO_4^{2-} + 4\,H_2O \tag{18}$$

The kinetic data for the reaction from several research groups is given in Table 1, with the assumption of first order kinetics respective to both components.

Experimental data measured with the microcalorimeter based on the LTF-MS reactor from LTF's MR-Lab series are used to further validate the application of reactor power estimation. The microcalorimeter itself consists of the commercially available plate microreactor, twelve Seebeck elements (SEs), a temperature-controlled base plate, a sealing block, a view glass, a top frame, and a stabilizing plate at the bottom. The base plate forms the foundation of the

Table 1 Thermokinetic data of the thiosulfate oxidation by different authors with the assumption of a first order reaction in respect to sodium thiosulfate and hydrogen peroxide

Author	ΔH_r [kJ mol^{-1}]	k_0 [m^3 kmol^{-1} s^{-1}]	E_A [kJ mol^{-1}]
Cohen and Spencer [40]	−552.3	$6.85 \cdot 10^{11}$	76.68
Lo and Cholette [41]	−586.2	$2.13 \cdot 10^{10}$	68.50
Lin and Wu [42]	−586.2	$2.00 \cdot 10^{10}$	68.50
Grau, Nougués and Puigjaner [43]	−586.2	$8.13 \cdot 10^{10}$	76.13
Frede, Greive and Kockmann [26]	−594.3	$2.66 \cdot 10^{9}$	62.20

microcalorimeter and provides a reference temperature for the SEs, which is required for accurate measurements. Therefore, a meander-shaped cooling channel is milled into the bottom side, through which a coolant is guided. A sealing block is mounted to the base plate from below via a stainless steel subplate to seal the cooling channel and provides boreholes for connection ports for the in- and outlet of the coolant. The horizontal dimensions of the sealing block and the subplate math those of the base plate. On top of the base plate, the SEs are sandwiched between the base plate and the microreactor. The position of the SEs follows the course of the reaction channel to obtain locally resolved heat flux profiles. In addition, the microcalorimeter is placed into a temperature-controlled closed box to minimize environmental influences.

For the experiments, all desired temperature and flow rates were set automatically, with certain waiting times to allow for heating and cooling of the whole systems. Steady-state measurements of the respective experimental settings were performed and every measurement point was recorded in triplets. Prior to the experiments, the SEs have been calibrated and baseline signal of the SEs have been recorded. Further and more detailed information can be found in [26] on the experimental procedure and the calorimetric measurement method itself.

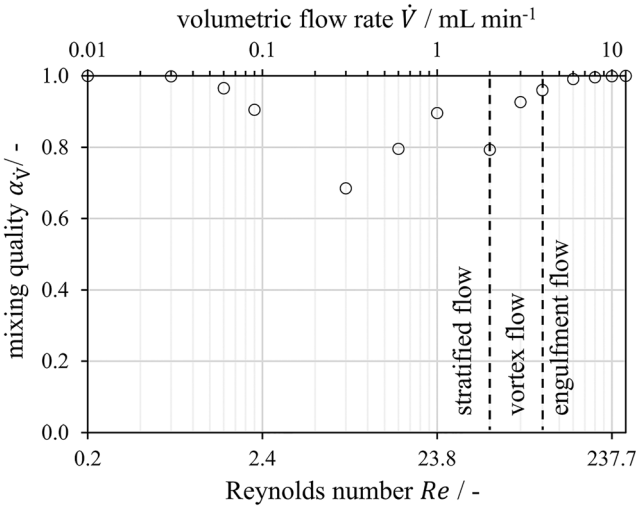

Fig. 8 Velocity-weighted mixing quality in the LTF-MS reactor for varying volumetric flow rates in different flow regimes and corresponding *Re* numbers

Results and discussion

Hydrodynamic studies

The velocity-weighted mixing quality in the LTF-MS reactor is calculated and discussed with focus on the corresponding flow regimes, as shown in Fig. 8. The calculation of the velocity-weighted mixing quality is given in the SI.

While stratified flow regime is observed for Reynolds numbers between 0.01 and 1 mL min^{-1}, stable vortices appear for $\dot{V} \geq 2$ mL min^{-1}. Symmetry breakup and engulfment flow is reached for $\dot{V} \geq 4$ mL min^{-1}. The corresponding streamlines are given in the SI for the flow regimes. For $\dot{V} = 2$ mL min^{-1}, a drop in the mixing quality occurs due to a switch in the ratio of diffusive to convective mixing. Diffusive mass transfer dominates in the retention volume for $\dot{V} = 1$ mL min^{-1}, where no vortices appear, due the microreactor's geometry. Convective mixing is not as strong as diffusive mixing in the retention volume. For $\dot{V} = 2$ mL min^{-1}, a shorter residence time is available for diffusion. Thus, the mixing quality decreases until larger vortices appear and the mixing process intensifies.

In Fig. 9, the RTD curves with the mean residence time and the corresponding variance of the second periodic mixing element are presented for volumetric flow rates of $\dot{V} = 0.03$, 0.8, 2, and 12 mL min^{-1}. The variance indicates the broadness of the distribution functions.

High fluctuations in the residence time can be seen at $\dot{V} = 0.03$ mL min^{-1} (top left diagram in Fig. 9). In the stratified flow regime, radial diffusion leads to deviations in the age at the outlet and to fluctuations in the RTD. The largest variance of 232 s^2 indicates the broadest distribution in stratified flow. With increasing convection for $\dot{V} = 0.8$ mL min^{-1} and stable vortex flow for $\dot{V} = 2$ mL min^{-1} only small fluctuations are evident in the tail. The distribution narrows due to laminar flow with less diffusion, higher convection, and low backflow. With a narrow residence time distribution, the stable vortex flow regime is favorable for parallel or serial chemical reactions, which require a well-controlled system. In the engulfment flow regime for $\dot{V} = 12$ mL min^{-1}, small peaks are present in the tail and the variance increases. Hence, the distribution broadens due to increased recirculation and backflow. However, the RTD curves do not indicate any spatial

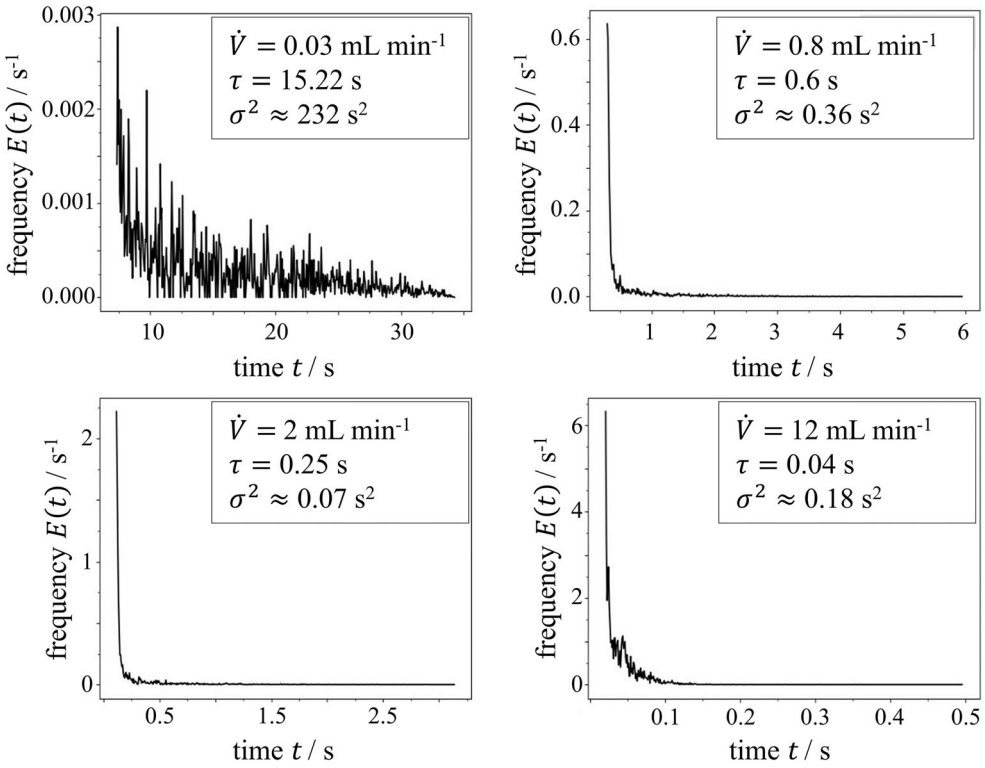

Fig. 9 RTD function with calculated mean residence time and variance after the second periodic mixing element in the LTF-MS reactor for varying volumetric flow rate

positions of the recirculation zones or backflow regions. Therefore, the corresponding mean age contour plots are displayed in Fig. 10.

For $\dot{V}$ = 0.03 mL min^{-1}, higher values age values at the walls and lower values in the middle of the channel indicate a laminar flow profile. The diffusive flow is clearly visible by the spread gradient in radial direction. Stagnation zones in the meandering bends lead to a higher age and thus an increased residence time. When increasing the flow rate up to $\dot{V}$ = 0.8 mL min^{-1}, these effects decrease. Still, the age is highest at the walls in the stagnation zones, but the radial gradient is less visible because convection is now dominating in comparison to diffusion. Only in the stagnation zones diffusive processes are indicated by the gradients. In the vortex flow regime for $\dot{V}$ = 2 mL min^{-1}, strong gradients are not visible anymore. However, vortices and recirculation zones can be clearly determined by higher age values. In the engulfment flow regime for $\dot{V}$ = 12 mL min^{-1}, the vortices are perfectly visible and even the location of the vortex cores is spatially resolved. The thin light stripes within the age contour plot indicate the locations of backflow in the channel.

Besides the spatially resolved fluid effects, the run time of the steady state simulation with the age variable was much faster than a transient simulation with injected tracer material.

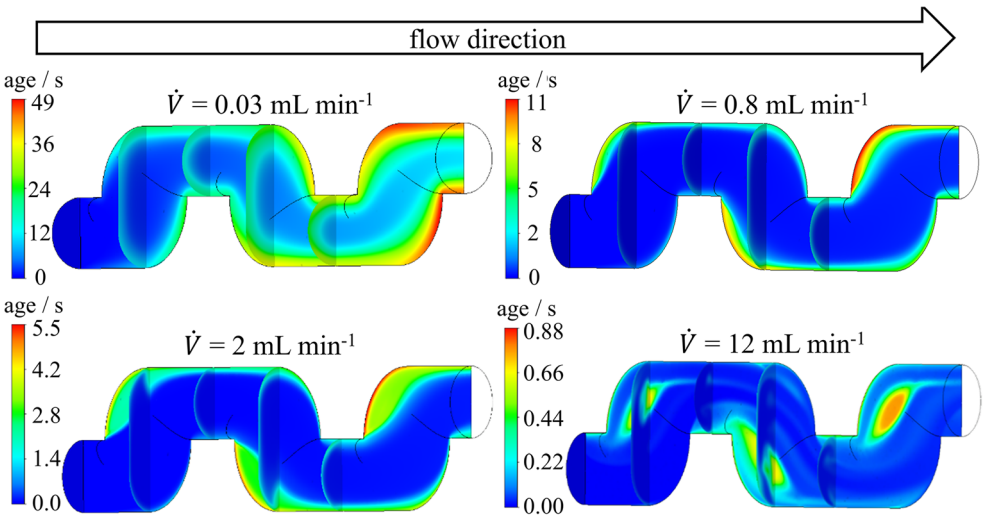

Fig. 10 Mean age contour plot after the second periodic mixing element in the LTF-MS reactor for varying volumetric flow rates and with flow direction from left to right

A comparison for a volumetric flow rate of 8 mL min^{-1} showed that the solution time of one periodic mixing element took 5–7 minutes on a workstation using 20 cores with an age variable, while the transient test simulation took 40–45 minutes on the same workstation. Therefore, the steady state simulation was almost 9 times faster than the transient one.

All in all, the mean age contour plots offer several advantages in comparison to the RTD curves when investigating flow behavior in micro channels. The contour plots do not only provide similar insights into the flow effects like vortices, recirculation zones or short-circuiting paths, but additionally spatially resolve them. This is especially beneficial for designing microstructured devices. Furthermore, steady state solutions with an additional age variable are obtained much faster than with transient simulations.

Reactor performance estimation

Prediction of conversion and temperature profiles

Conversion and temperature profiles for the oxidation of sodium thiosulfate are estimated using kinetic data provided by Lo and Cholette [41] and Grau et al. [43]. These two kinetic datasets are chosen as they differ the most in the newer datasets, as shown in Tab. 1. Thus, the largest possible design space is predicted. The same experimental parameters were chosen as in the experiments performed by Frede et al. [26], in order to further compare the prediction with experimental data. The inlet and ambient temperatures were set to 25 °C and concentrations of c_{NaTS} = 1.0 M and c_{HP} = 2.2 M were used. Here, it is important to mention that it is assumed that the flow profile does not change due to the reaction. The respective conversion and temperature profiles are shown in Fig. 11 for the LTF-MS reactor and varying volumetric flow rates.

In general, the conversion increases over the reactor length as expected. For kinetic data by Lo and Cholette [41], full conversion occurs for volumetric flow rates between 0.01 and 0.6 mL min^{-1}. Increasing the flow rate leads to a lower conversion as residence time is reduced, as can be seen for $\dot{V}$ = 1 mL min^{-1}. The corresponding temperature profiles show that peaks appear at conversion rates higher than 80% for flow rates with full conversion. With increasing flow rate, the temperature peaks are higher, since more heat is released by the reaction of more material. In addition, the peak shifts to the reactor outlet due to the reduced residence time, which pushes the reaction out of the reactor. For $\dot{V}$ = 1 mL min^{-1}, a continuously increasing temperature profile can be observed without a peak, as the conversion rate is below 80%. For kinetic data by Grau et al. [43], complete conversion is not achieved with any volume flow. The highest conversion of approximately 0.8 is achieved at the lowest flow rate with correspondingly highest residence time. The corresponding temperature profiles feature a peak at conversion rates of 40%. For flow rates with conversion rates below 40%, a continuously increasing

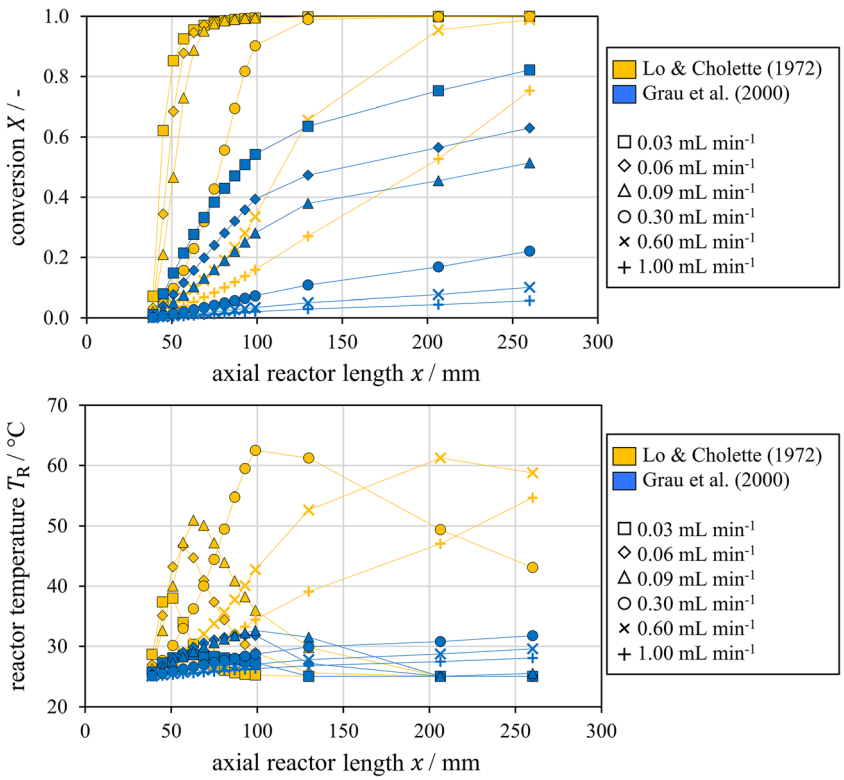

Fig. 11 Predicted conversion and temperature profile in the LTF-MS reactor with kinetic parameters of Lo & Cholette [41] and Grau et al. [43] for $c_{NaTS,\,0}$ = 1 M and T_{in} = $T_{ambient}$ = 25 °C and different volumetric flow rates

temperature profile can be observed. The generally lower conversion rates and temperatures compared to Lo and Cholette [41] are due to the higher activation energy determined by Grau et al. [43]. This leads to a lower kinetic coefficient and consequently to lower conversion rates under identical conditions. Moreover, heat effects have a minor role, which would otherwise also accelerate the reaction due to the heat effects considered within the prediction. Based on these observations, volumetric flow rates in the range of 0.03 to 0.09 mL min^{-1} are of interest for calorimetric measurements to determine thermokinetic data, since complete conversion according to Lo and Cholette [41] or the highest conversion rates according to Grau et al. [43] are expected there.

Comparison with data from microcalorimeter

In Fig. 12, the predicted conversion and temperature profiles are compared to experimental data obtained in our microcalorimeter within the above mentioned range of 0.03 to 0.09 mL min^{-1}.

The experimentally determined conversion profiles show a very similar pattern to the predicted profiles with kinetic data from Lo and Cholette [41]. However, some deviations can be seen. In general, the conversion profiles are shifted to the right towards the reactor outlet. In addition, full conversion is not observed for $\dot{V}$ = 0.3 mL min^{-1}, as the reaction progress increases only slightly after 150 mm. The same agreement is observed for the temperature profiles with a shift to the right. The shift was expected, as the kinetic data already showed a small deviation. As with the conversion profile, a larger deviation is observed for $\dot{V}$ = 0.3 mL min^{-1}. At this point, it should be explicitly pointed out again that the temperature in the experiments is determined by local energy balances of the individual Seebeck elements. These cannot replace a local temperature measurement, since various assumptions e.g. regarding the heat loss strongly influence the results. Only a rough estimation of the temperature is made. On one hand, the deviation of the peak height is higher than for the other volume flows and, on the other hand, fluctuations become visible in the temperature profile after 150 mm. The fluctuations of the temperature observed for $\dot{V}$ = 0.3 mL min^{-1} were also observed by Frede et al. [26] at a volumetric flow rate of approximately 0.2 mL min^{-1}. There, heat flux profiles are measured, where a fluctuating profile was observed after SE6. After SE6, the reaction channel features a 90° bend above SE7. This results not only in a higher projection area, which in turn results in a higher measured heat flux, but can also result in improved mixing [44, 45]. Therefore, the mixing structure along the reactor and above the SEs should be as uniform as possible to minimize such effects. Although the activation energy determined in our microcalorimeter is lower, the pre-exponential factor is also lower resulting in a lower kinetic coefficient. In addition, the reactor performance estimation evaluates in small reactor segments, which generally increases the accuracy of the prediction.

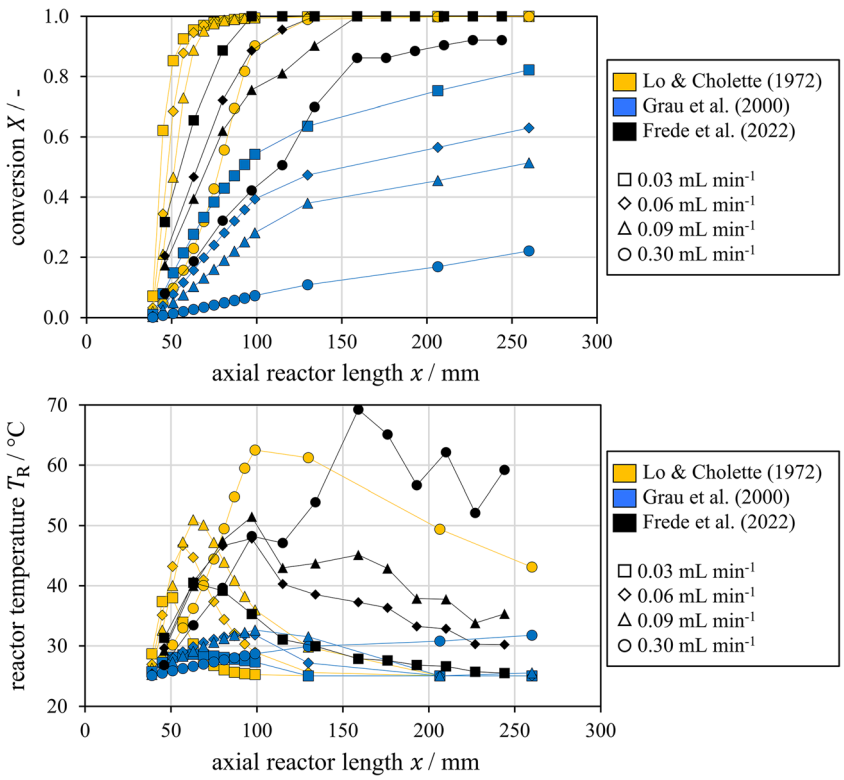

Fig. 12 Comparison of experimental data by Frede et al. [26] and predicted conversion and temperature in the LTF-MS reactor with kinetic parameters of Lo & Cholette [41] and Grau et al. [43] for $c_{NaTS,\,0}$ = 1 M and T_{in} = $T_{ambient}$ = 25 °C and different volumetric flow rates

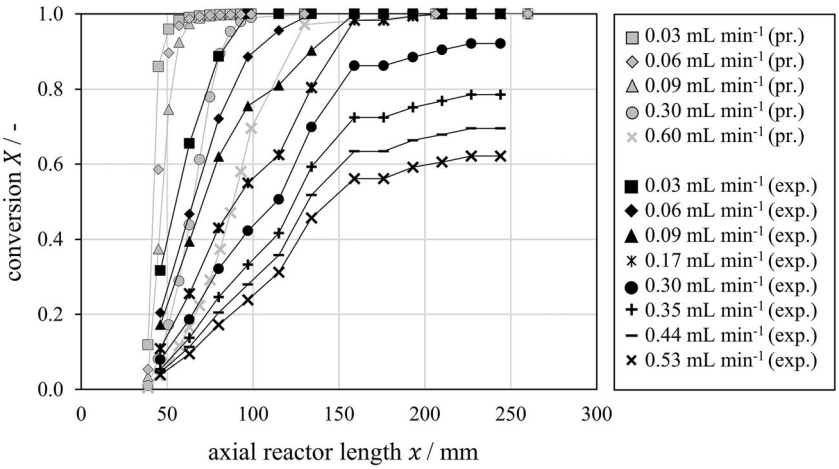

Fig. 13 Comparison of experimental data by Frede et al. [26] (exp.) and predicted conversion reactor with kinetic parameters of Frede et al. [26] (pr.) in the LTF-MS

Validation of reactor performance estimation

To validate our approach, we compared the predicted conversion and temperature profiles with the determined kinetic data in our calorimeter and the experimentally determined profiles, as shown in Fig. 13.

Based on Fig. 13, it can be seen that the reactor performance estimation predicts full conversion in the reactor for the kinetic data of Frede et al. [26] for volumetric flow rates up to and including 0.6 mL min^{-1}. For the experimental data, however, it is observed that complete conversion is no longer achieved for volumetric flow rates of 0.3 mL min^{-1} and higher. Of course, the fact that the reactor performance estimation no longer considers the exact mixing behavior, but the mean residence time, comes into play here. As shown in Fig. 8, the mixing quality is below 0.9 for flow rates higher than 0.1 mL min^{-1}. Hence, complete mixing cannot longer be assumed. This also explains the increasing deviation for volumetric flow rates of 0.3 mL min^{-1} and higher.

All in all, the calculations of conversion and temperature profiles lead to good agreement with experimental results with this approach for volumetric flow rates up to 0.17 mL min^{-1} and enable predictions of suitable experimental settings for the LTF-MS reactor. The kinetic data can be easily varied, since only the reactor performance has to be recalculated, not the flow behavior with residence time distribution. Hence, this approach can be used to determine suitable experimental settings when investigating exothermic reactions as it provides an initial estimate of how the reaction is going to behave within the reactor assuming different kinetics. The subsequent comparison of the conversion and temperature profiles then allows conclusions to be drawn about the kinetics without having to determine them explicitly. In addition, inlet concentration and temperature can be varied to predict suitable experimental ranges more accurate. The resulting sensitivity analysis can also be used for first safety estimation of the reactor or detailed design of experiments.

Conclusion

The investigation of the dynamic behavior within a reactor in kinetic studies is a crucial step to increase efficiency and effectiveness in chemical process development. Hence, the use of simulation tools such as CFD is essential to accompany kinetic studies and to optimize them with regard to their design. In this study, a hybrid modelling approach was presented, combining CFD simulations with conventional reactor models, to predict chemical conversion and temperature profiles of chemical reactions within a microreactor employed in a reaction calorimeter. The microreactor was divided into smaller compartments with symmetry planes reducing the computational effort and enabling simulations on conventional workstation independent of high-performance computing. The mean age theory was implemented in ANSYS CFX with an additional variable enabling steady-state simulations to obtain RTD data up to nine times faster than with transient flow simulations. Automation scripts were developed to accelerate simulations, CFX-Post operations, data handling and calculations leading to a total simulation time of one to four hours depending on the volumetric flow rate on a workstation with 20 cores. The approach was successfully tested for the oxidation of sodium thiosulfate, comparing experimentally determined conversion and temperature profiles to predict those using two different kinetic data sets given in literature.

If a higher precision of the developed method is desired, a higher number of cross-sectional planes can be inserted, from which concentration and age profiles are extracted. This leads to a higher resolution of the temperature profiles over each reactor compartment and a more accurate description of heat effects with higher computational effort. The accuracy of the predictions can be enhanced even further with a better description of heat loss by exact heat transfer coefficients for the reactor compartments.

However, the approach can provide useful information for the design of experiments when investigating exothermic reactions, whose kinetic data have not yet been determined in continuous flow and in microscale. In future work, we will test the reactor performance estimation for further reactions such as esterification of acetic anhydride by methanol, which is well documented in the literature. The decoupling of hydrodynamics and reaction kinetics enables the development of a database for experimental planning. This enables the user to target experimental parameters that are suitable for calorimetric measurements without performing experiments in advance.

Symbols

c	[mol m^{-3}]	concentration
$c_{A,0}$	[mol m^{-3}]	starting concentration of limiting component A
c_0	[mol m^{-3}]	starting concentration
c_p	[J kg^{-1} K^{-1}]	specific heat capacity
D	[m^2 s^{-1}]	diffusion coefficient
$E(t)$	[s^{-1}]	residence time distribution
E_A	[J mol^{-1}]	activation energy
$F(t)$	[s]	cumulative residence time distribution
$\widetilde{F}$	[s]	cumulative spatial age distribution
$\widetilde{f}$	[kg m^{-1} s^{-2}]	spatial age distribution
H_r	[J mol^{-1}]	molar reaction enthalpy
k	[(m^3 mol^{-1})$^{m-1}$ s^{-1}]	reaction rate coefficient
k_0	[(m^3 mol^{-1})$^{m-1}$ s^{-1}]	pre-exponential factor in Arrhenius kinetic
k_{ht}	[W K^{-1}]	area specific heat transfer coefficient
m	[−]	reaction order
p	[Pa]	pressure
$\dot{Q}_{loss}$	[W]	heat loss
R	[J mol^{-1} K^{-1}]	universal gas constant
T	[K]	temperature
T_{ad}	[K]	adiabatic temperature rise
$T_{ambient}$	[K]	ambient temperature
T_{ave}	[K]	average temperature in a compartment
T_i	[K]	outlet temperature of the compartment
T_{in}	[K]	inlet temperature
T_{i-1}	[K]	inlet temperature of the compartment
t	[s]	time
u	[m s^{-1}]	velocity
$\overline{u}$	[m s^{-1}]	average velocity
$\overrightarrow{u}$	[m s^{-1}]	velocity vector
$\dot{V}$	[m^3 s^{-1}]	volumetric flow rate
X	[−]	conversion
$\overline{X}$	[−]	mean conversion
$X_{i,temp}$	[−]	temporary conversion during iteration
x	[m]	axial reactor coordinate

Dimensionless numbers

Da_1	$Da_1 = \frac{\tau_h}{t_r}$	first Damköhler number
Da_2	$Da_2 = \frac{\tau_D}{t_r}$	second Damköhler number
Re	$Re = \frac{\overline{u}d\rho}{\eta}$	Reynolds number

Greek symbols

α	[s]	age
$\overline{\alpha}$	[s]	mean age
$\alpha_{\dot{V}}$	[−]	velocity-weighted mixing quality
η	[Pa s]	dynamic viscosity
ρ	[kg m^{-3}]	density
τ	[s]	residence time
τ_h	[s]	hydraulic residence time
σ^2	[−]	variance
∇	[−]	nabla operator

Abbreviations CFD, Computational Fluid Dynamics; FTIR, Fourier–transform infrared spectroscopy; HP, hydrogen peroxide; HPLC, high-performance liquid chromatography; LFR, laminar flow reactor; LTF, Little Things Factory; NaTS, sodium thiosulfate; RMS, root-mean-square; RTD, residence time distribution; SE, Seebeck element

Supplementary Information The online version contains supplementary material available at https://doi.org/10.1007/s41981-022-00251-z.

Acknowledgments Special T.A.F. thanks the networking program 'Sustainable Chemical Synthesis 2.0' (SusChemSys 2.0) for the support and fruitful discussions across disciplines.

Funding Open Access funding enabled and organized by Projekt DEAL. This research of the Forschungsvereinigung Forschungs-Gesellschaft Verfahrens-Technik e.V. (GVT) was funded by the German Federal Ministry of Economic Affairs and Climate Action (BMWK) via the Arbeitsgemeinschaft Industrieller Forschungsvereinigungen (AiF) within the framework of the program for the promotion of the Industrielle Gemeinschaftsforschung (IGF), grant number IGF no. 20819 N.

Declarations

Competing interests The authors have no competing interests to declare that are relevant to the content of this article.

References

1. Moore JS, Jensen KF (2014). Angew Chem Int Ed 53(2):470–473. https://doi.org/10.1002/anie.201306468
2. Moore JS, Smith CD, Jensen KF (2016). React Chem Eng 1(3): 272–279. https://doi.org/10.1039/c6re00007j
3. Schwolow S, Braun F, Rädle M, Kockmann N, Röder T (2015). Org Process Res Dev 19(9):1286–1292. https://doi.org/10.1021/acs.oprd.5b00184
4. Mozharov S, Nordon A, Littlejohn D, Wiles C, Watts P, Dallin P, Girkin JM (2011). J Am Chem Soc 133(10):3601–3608. https://doi.org/10.1021/ja1102234
5. Hone CA, Holmes N, Akien GR, Bourne RA, Muller FL (2017). React Chem Eng 2(2):103–108. https://doi.org/10.1039/c6re00109b
6. Haas CP, Biesenroth S, Buckenmaier S, Van De Goor T, Tallarek U (2020). React Chem Eng 5(5):912–920. https://doi.org/10.1039/d0re00066c
7. Waldron C, Pankajakshan A, Quaglio M, Cao E, Galvanin F, Gavriilidis A (2020). React Chem Eng 5(1):112–123. https://doi.org/10.1039/c9re00342h
8. Fath V, Lau P, Greve C, Kockmann N, Röder T (2020). Org Process Res Dev 24(10):1955–1968. https://doi.org/10.1021/acs.oprd.0c00037
9. Ładosz A, Kuhnle C, Jensen KF (2020). React Chem Eng 5(11): 2115–2122. https://doi.org/10.1039/d0re00304b
10. Antes J, Krause H, Löbbecke S, Schifferdecker D (2004) Method and device for measuring the heat developed by chemical or physical reactions, EU Patent 20040027615
11. Antes J, Schifferdecker D, Krause H, Loebbecke S (2004). Chem Ing Tech 76(9):1332–1333
12. Antes J, Gegenheimer M, Krause H, Löbbecke S, Wirker R, Knorr A (2008). Chem Ing Tech 80(9):1270–1270. https://doi.org/10.1002/cite.200750657
13. Reichmann F, Millhoff S, Jirmann Y, Kockmann N (2017). Chem Eng Technol 40(11):2144–2154. https://doi.org/10.1002/ceat.201700419
14. Reichmann F, Vennemann K, Frede TA, Kockmann N (2019). Chem Ing Tech 91(5):622–631. https://doi.org/10.1002/cite.201800169
15. Frede TA, Burke I, Kockmann N (2021). Chem Ing Tech 93(5): 802–808. https://doi.org/10.1002/cite.202000223
16. Maier MC, Leitner M, Kappe CO, Gruber-Woelfler H (2020). React Chem Eng 5(8):1410–1420. https://doi.org/10.1039/d0re00122h
17. Mortzfeld F, Polenk J, Guelat B, Venturoni F, Schenkel B, Filipponi P (2020). Org Process Res Dev 24(10):2004–2016. https://doi.org/10.1021/acs.oprd.0c00117
18. Moser M, Georg AG, Steinemann FL, Rütti DP, Meier DM (2021). J Flow Chem 11(3):691–699. https://doi.org/10.1007/s41981-021-00204-y
19. Schneider MA, Stoessel F (2005). Chem Eng J 115(1–2):73–83. https://doi.org/10.1016/j.cej.2005.09.019
20. Sen MA, Kowalski GJ, Fiering J, Larson D (2015). Thermochim Acta 603:184–196. https://doi.org/10.1016/j.tca.2014.09.024
21. Nieves-Remacha MJ, Kulkarni AA, Jensen KF (2015). Ind Eng Chem Res 54(30):7543–7553. https://doi.org/10.1021/acs.iecr.5b00232
22. Khaydarov V, Borovinskaya ES, Reschetilowski W (2018). Appl Sci 8(12):3–6. https://doi.org/10.3390/app8122458
23. Asano S, Yatabe S, Maki T, Mae K (2019). Org Process Res Dev 23(5):807–817. https://doi.org/10.1021/acs.oprd.8b00356
24. Jourdan N, Neveux T, Potier O, Kanniche M, Wicks J, Nopens I, Rehman U, Le Moullec Y (2019). Chem Eng Sci:210. https://doi.org/10.1016/j.ces.2019.115196
25. Cremer-Bujara E, Biessey P, Grünewald M (2020). Macromol React Eng 14(1):1–11. https://doi.org/10.1002/mren.201900034
26. Frede TA, Greive M (2022). N Kockmann 3(4):525–536. https://doi.org/10.3390/reactions3040035
27. Frede TA, Dietz M, Kockmann N (2021). J Flow Chem 11(3):321–332. https://doi.org/10.1007/s41981-021-00145-6
28. Stiles PJ, Fletcher DF (2003). Phys Chem Chem Phys 5(6):1219–1224. https://doi.org/10.1039/b211686c
29. Spalding DB (1958). Chem Eng Sci 9(1):74–77
30. Sandberg M (1981). Build Environ 16(2):123–135. https://doi.org/10.1016/0360-1323(81)90028-7
31. Liu M, Tilton JN (2010). AIChE J 56(10):2561–2572
32. LEAP CFD Team (2014) Tips & tricks: calculating the mean age of air for HVAC simulations in ANSYS CFD. https://www.computationalfluiddynamics.com.au/tips-tricks-calculating-mean-age-of-air-with-cfd/. Accessed Oct 26 2022
33. Galletti C, Roudgar M, Brunazzi E, Mauri R (2012). Chem Eng J 185–186(0):300–313. https://doi.org/10.1016/j.cej.2012.01.046
34. Ferziger JH, Peric M (2002) Computational methods for fluid dynamics3rd edn. Springer, Berlin, Heidelberg
35. Danckwerts PV (1952). Appl Sci Res Sect A 3(4):279–296. https://doi.org/10.1007/BF03184936
36. Fogler HS, Gürmen MN (2006) Elements of chemical reaction engineering4th edn. Pearson Education Internat, Upper Saddle River, NJ
37. Levenspiel O (**1999**) Chemical Reaction Engineering3rd edn. John Wiley & Sons
38. Hagen J (2004) Chemie Reaktoren Auslegung Und Simulation. Wiley-VCH, Weinheim
39. Baerns M, Behr A, Brehm A, Gmehling J, Hofmamm H, Onken U, Reknken A, Hinrichsen K-O, Palkovits R (2013) Technische Chemie2nd edn. Wiley-VCH, Weinheim
40. Cohen WC, Spencer JL (1962). Chem Eng Prog 58(12):40–41
41. Lo SN, Cholette A (1972). Can J Chem Eng:50
42. Lin KF, Wu LL (1981). Chem Eng Sci 36(2):435–444. https://doi.org/10.1016/0009-2509(81)85026-9
43. Grau MD, Nougués JM, Puigjaner L (2000). Chem Eng Process 39(2):141–148. https://doi.org/10.1016/S0255-2701(99)00015-X
44. Dean WR (1927). Philos Mag 7:208–223
45. Dean WR (1928). Philos Mag 7:673–695